Purely entropic self-assembly of the bicontinuous Ia$\overline{3}$d gyroid phase in equilibrium hard-pear systems

SCHÖNHÖFER, Philipp W. A., ELLISON, Laurence J., MARECHAL, Matthieu, CLEAVER, Douglas J. <http://orcid.org/0000-0002-4278-0098> and SCHRÖDER-TURK, Gerd E.

Citation:

Purely Entropic Self-Assembly of the Bicontinuous Ia3̄d Gyroid-Phase in Equilibrium Hard-Pear Systems

Philipp W. A. Schönhöfer[1,2,*], *Laurence J.* Ellison[3,*], *Matthieu* Marechal[2], *Douglas J.* Cleaver[3,**], and *Gerd E.* Schröder-Turk[1,***]

[1] *School of Engineering and Information Technology, Mathematics & Statistics, Murdoch University, 90 South Street, Murdoch, WA 6150, Australia*
[2] *Institut für Theoretische Physik I, Universität Erlangen-Nürnberg, Staudtstraße 7, 91058 Erlangen, Germany*
[3] *Materials and Engineering Research Institute, Sheffield Hallam University, Sheffield S1 1WB, United Kingdom*

Abstract. We investigate a model of hard pear-shaped particles which forms the bicontinuous Ia3̄d structure by entropic self assembly, extending the previous observations of Barmes *et al.* [PRE **68**, 021708 (2003)] and Ellison *et al.* [PRL **97**, 237801 (2006)]. We specifically provide the complete phase diagram of this system, with global density and particle shape as the two variable parameters, incorporating the gyroid phase as well as disordered isotropic, smectic and nematic phases. The phase diagram is obtained by two methods, one being a compression-decompression study and the other being a continuous change of the particle shape parameter at constant density. Additionally, we probe the mechanism by which interdigitating sheets of pears in these systems create surfaces with negative Gauss curvature, which is needed to form the Gyroid minimal surface. This is achieved by use of Voronoi tessellation, whereby both the shape and volume of Voronoi cells can be assesed in regard to the local Gauss curvature of the Gyroid minimal surface. Through this, we show that the mechanisms prevalent in this entropy-driven system differ from those found in systems which form Gyroid structures in nature (lipid bilayers) and from synthesised materials (di-block copolymers) and where the formation of the Gyroid is enthalpically driven. We further argue that the Gyroid phase formed in these systems is a realisation of a modulated splay-bend phase in which the conventional nematic has been predicted to be destabilised at the mesoscale due to molecular-scale coupling of polar and orientational degrees of freedom.

1 Introduction

This article addresses the spontaneous formation of one of nature's most symmetric, most complex and most ordered structures – the self-assembled bicontinous Gyroid structure. Further, it does so in the context of a system which involves no attractive forces. Therefore, the formation of this Gyroid structure does not happen despite entropy, but because of it: the long-range order emerges precisely because this highly ordered structure maximises entropy. Whilst this runs counter to the commonly held, but flawed, notion that maximal entropy is always associated with increasing levels of disorder [1–3], in fact, several examples of entropy-driven ordering have been previously identified. Foremost amongst these are the celebrated ordering transition in the hard sphere equilibrium fluid [4, 5], beautifully realised in colloidal crystals by Pusey and van Megen [6], and the longstanding debate about the corresponding hard disk system [7, 8], as well as the emergence of nematic or smectic order in simple liquid crystal models like spherocylinders [9–11], ellipsoids [12], helices [13] and other multi-sphere objects [14, 15] . See also the recent review by Manoharan *et al.* [16].

This article analyses the formation of the double Gyroid in equilibrium ensembles of hard pear-shaped particles, thereby extending earlier work by Barmes *et al.* [17] and Ellison *et al.* [18]. Pear-shaped particles are tapered versions of spheroids, best thought of as prolate ellipsoids with a wider 'blunt' end and a narrower 'sharp' end (see Figure 1). For appropriate parameter values, equilibrium ensembles of such pear-shaped particles adopt the so-called double Gyroid structure [19–21]. The double Gyroid is a bicontinuous geometry that is best visualised as two intertwined, identical, periodic and highly symmetric network-like or labyrinth-like domains (see [22] for animation). The common interface between these domains is a triply-periodic, saddle-shaped surface, with symmetry group *Ia3̄d* including operations that exchange the two labyrinth-like domains. The pears adopt this diffusive phase in an arrangement that fills space fairly uniformly, at fluid-like densities. The blunt ends of the pears point into the labyrinthine domains, with pear positions adopting a distribution of distances from the (hypothetical) minimal surface and pear orientations adopting characteristic
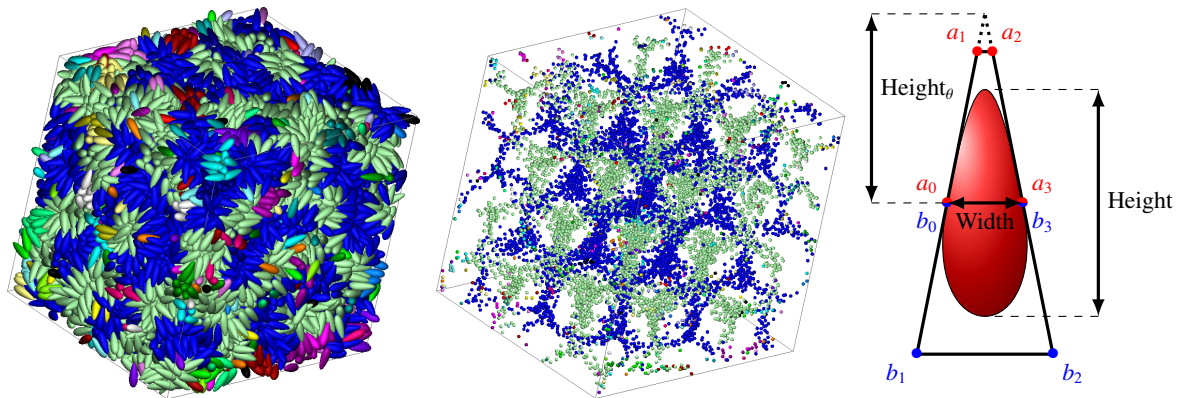

Figure 1. Left: an assembly of 10000 pear-shaped particles forming the Gyroid structure ($k_\theta = 3.8$, $\rho_g = 0.57$). Center: positions of the blunt ends of the pears, depicted by spheres which are color coded to show distinct clusters. Right: a single pear-shaped particle, characterised by its aspect ratio $k = \frac{\text{Height}}{\text{Width}}$ and tapering parameter $k_\theta = \frac{\text{Height}_\theta}{\text{Width}}$. The tapering angle is given by $\theta = 2\arctan(\frac{1}{2k_\theta})$. The marks a_i and b_i are the control points of the Bézier curves which are used to fit the pear shape.

angles around the minimal surface normal directions. The pear blunt ends, hence, can straightforwardly be subdivided into two subsets, each occupying one or the other of the labyrinthine domains, whereas the locations of the sharp ends are staggered near the minimal surface, see Figure 2b.
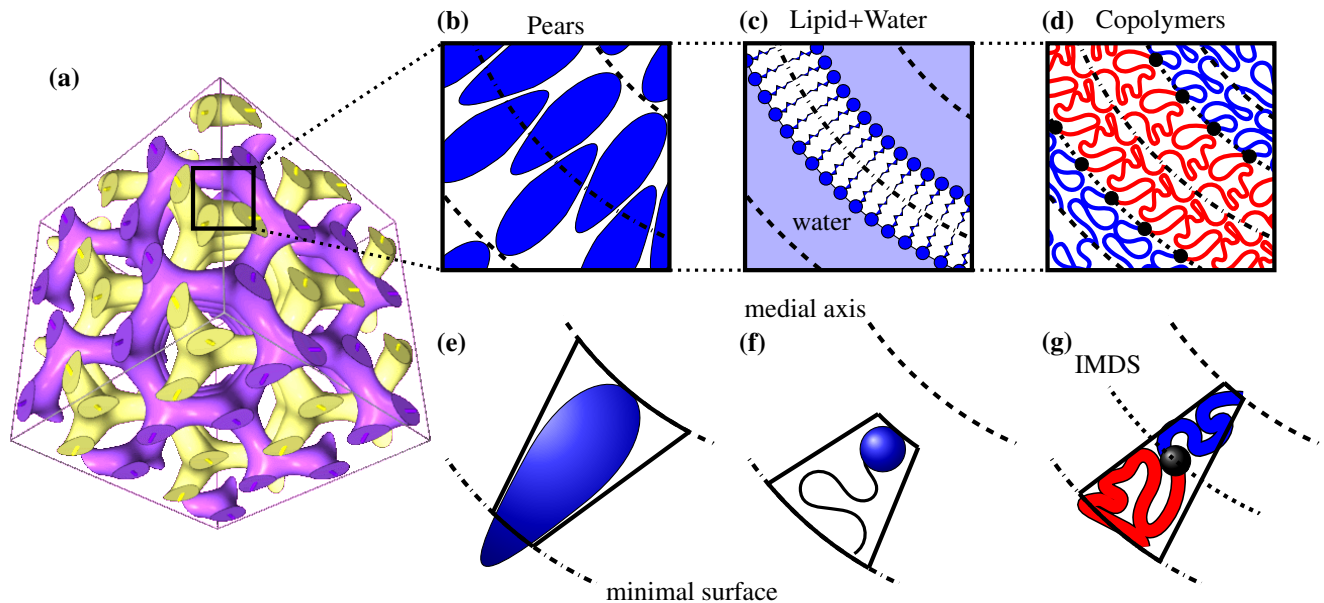

Figure 2. The three different arrangements within the Gyroid phase (a) generated by: tapered liquid crystalline pears (b); lipids in a mixture with water (c); and di-block copolymers (d). The lipids and copolymers follow Steiner's theorem and taper towards the medial axis (f+g) and the inter-material dividing surface (IMDS) (g). In contrast, the pears form interpenetrating bilayers and, consequently, get wider as they approach the medial axis (e).

In various forms, the double Gyroid is a commonly observed phase in a variety of self-assembled soft matter systems [22–24]. In particular, systems of amphiphilic molecules – with energetic terms that favour local segregation – adopt the double Gyroid: in the inverse lipid/water phase, a warped bilayer membrane separates two aqueous domains [25–27], see Figure 2c. Also, dry monovalent soaps form double Q_I double Gyroid phases when their hydrophobic moieties form the network-like domains in the absence of water [28]. The second important classification of molecules that adopt double Gyroids are copolymeric melts [29], in particular, diblock copolymers. These form the double Gyroid phase at

volume fractions of approximately 33% of the minority component [30, 31], see Figure 2d. The double Gyroid has also recently been observed in experimental investigation of dendrimer systems [32] and simulations using sphero-symmetric potentials with short-range attractions and longer-range repulsions [33–35].

The importance of entropy for the self-assembly of amphiphilic systems has long been recognised, and is implicit in both the molecular shape concept [23, 36] and the Helfrich formalism [37, 38]. Indeed, soft matter physics is generally concerned with systems in which entropy plays a significant role, that is, where interaction terms are typically of the same order as the thermal energy $k_B T$. This is certainly the regime in which the bicontinuous double Gyroid phase is formed by amphiphilic molecules. However, all of the systems mentioned in the previous paragraph also have a clear enthalpic component, evident in the amphiphilic (segregating) nature of their constituent molecules. This is a significant difference from the hard pear-shaped particles studied here. One goal of this article is, therefore, to contribute to a deeper understanding of the mechanisms that lead to the formation of double Gyroid phases. Are the mechanisms in amphiphilic systems fundamentally different from those exhibited by pear-shaped particles? Is the mechanism by which the Gyroid phase increases the entropy in the pear-shaped system the same as that by which this happens in the amphiphilic systems? This article intends to provide data that will contribute to the resolution of these questions.

We also note that there is one particular way in which the behaviour of these pear-shaped systems is distinguished from those of other entropy-driven ordering processes such as those of hard spheres and liquid crystals. The onset of the double Gyroid phase creates crystallographic order on a larger length-scale ('meso-scale') than the particle or molecular scale, forming unit cells whose dimension is one or more orders of magnitude larger than the particle or molecule size. This contrasts with the ordered phases of hard spheres and liquid crystals where the crystallographic parameter corresponds to the translation from one particle to its nearest neighbour (and hence to the molecular scale itself). While the formation of emergent meso-scale order by self-assembly is by now a well established concept, a clear discrimination between the energetic and entropic contributions is an only partially understood question and one to which we aim to contribute here. Ultimately, understanding how entropy can be used to create ordered structures on the technologically important meso-scale (typically nanometers) is an essential step towards low-energy sustainable nano-engineering. 'Only entropy comes easy' [39].

This paper is structured as follows. In Section 2, we present the main simulation methodology and results that underpin this work and, thus, present a phase diagram showing the density-tapering parameter phase diagram of hard pears, including the extent of its Gyroid phase region. Following this, in section 3, detailed structural analysis is undertaken, through which insights are gained into the nature of the hard pear Gyroid and how it differs from those exhibited by different classes of experimental system. Finally, in the Conclusion, the entropy-driven Gyroid phase formed by the hard pear system is appraised in the round. Through this, a compelling argument is made that it is a realisation of a modulated splay-bend phase in which the conventional nematic has been predicted to be destabilised at the mesoscale due to molecular-scale coupling of polar and orientational degrees of freedom.

2 Phase Diagram

In this Section, we extend previous reports on the simulation of systems of hard pear-shaped particles. Barmes *et al.* showed that for long, tapered particles with aspect ratio $k = 5$ and $k_\theta = 5$ the nematic, bilayer smectic and crystalline phases are formed [17], see Figure 1 for the definitions of k and k_θ. For shorter particles, however, this initial study only found a "domain ordered" arrangement on compression of systems of 1,000 tapered particles. Subsequently, by simulating 10,000 particles with $k = 3$ and $k_\theta = 3.8$, Ellison *et al.* showed that, on compression from the isotropic fluid, the system was actually entering a Gyroid arrangement with long-range, three-dimensional periodicity [18]. The same study also showed spontaneous development of a Gyroid structure on expansion of a high density, interdigitated bilayer smectic, but the reverse transition was not observed.

We here use Molecular Dynamics (MD) and Monte Carlo (MC) simulation techniques to undertake a systematic simulation study of the ordering behaviour of $k = 3$ hard pears for a range of tapering angles. The interaction potential used to represent the hard core interaction for these pears is the modified version of the purely repulsive Weeks-Chandler-Andersen potential (WCA) [40], which Barmes *et al.* introduced. This is an implementation of the parametric hard Gaussian overlap (PHGO) approximation which is, in turn, based on the generalised Gay Berne interaction [41, 42]. The PHGO approach is founded on the observation that contacts between convex particles can locally be approximated by those between appropriately chosen ellipsoids. To maintain adherence to this, particle convexity is achieved here by using a core description defined by two continuously differentiable Bézier curves [17]. Each pear-pear interaction can then be described via an expansion based on multiple hard core ellipsoid potentials, weighted to mimic the Bézier descriptions at arbitrary relative orientation. Full details of the PHGO approach and its application to hard pear systems is given in Ref. [17, 43].
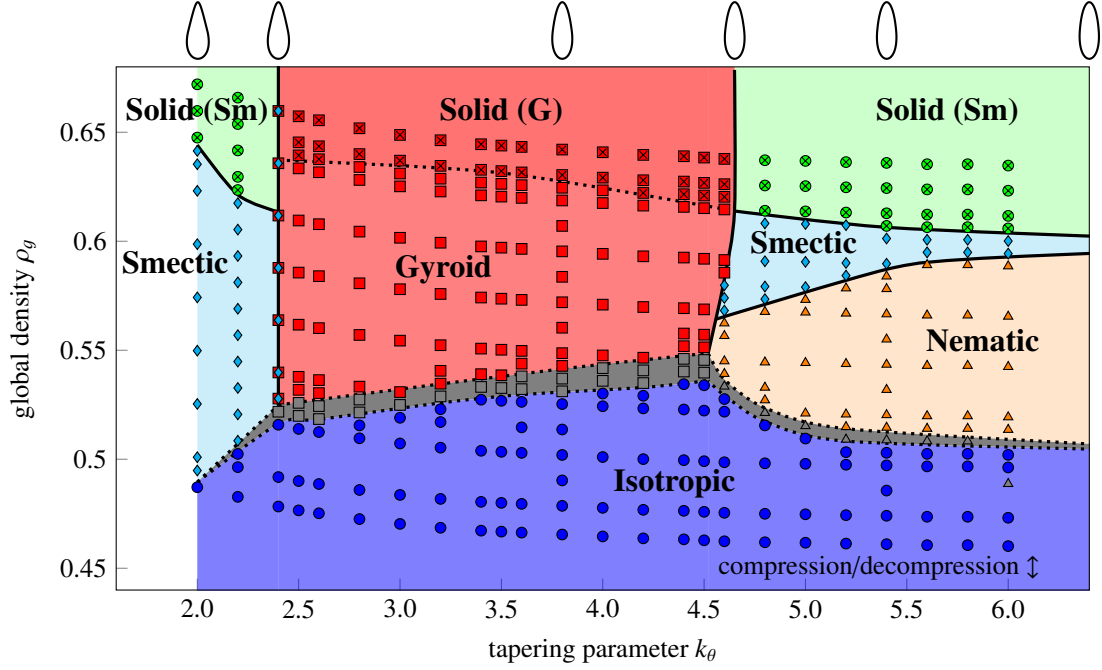
Figure 3. Phase diagram of hard pear-shaped particles with $k = 3.0$ obtained by compression (from isotropic) and decompression at fixed tapering parameter k_θ for systems of 3040 particles in a cubic simulation box. Gray regions between the isotropic and ordered phases indicate parameter values for which phase hysteresis is observed between compression and decompression sequences. The schematics above the graph indicate the cross-sectional shape of the particles associated with each k_θ value.

For this part of the study, simulations are performed on systems of $N = 3040$ particles with k_θ between 2.0 and 6.0 (tapering angle between 28.1° and 9.5°) within a cubic box with three dimensional periodic boundary conditions. The lower boundary of $k_\theta = 2$ is set to ensure that there is no particle concavity. Full simulation sets are performed using MD in the canonical (NVT) ensemble, with a time step $\Delta t = 0.0015$ and the dimensionless temperature T set to 1, since phase behaviour at fixed density is independent of the temperature for hard-particle systems [44]. Additionally, MC simulation sets using the same parameters are run for $k_\theta = 2.2$, $k_\theta = 3.8$ and $k_\theta = 5.4$ and for other systems as outlined in subsequent Sections. The MC translation step and the rotation step are set as $\Delta s = 0.005$ and $\Delta \phi = 0.2°$, respectively. The results of these two simulation sets show no significant differences. The global density of the system

$$\rho_g = \frac{N \cdot V_{pear}}{V_{box}}, \qquad (1)$$

which corresponds to the packing fraction, is defined by the pear volume V_{pear}, calculated numerically using a mesh of the particle's surface, and the volume of the simulation box V_{box}. Here, and subsequently, lengths are expressed in the units of the pear width at its waist w_p.

For each value of k_θ an initial, crystalline ordered configuration generated at low density ($\rho_g = 0.28$) is run to erase all configurational memory before being compressed to a starting density $\rho_g = 0.44$. Subsequently, a sequence of small compression steps are imposed (see symbols in Figure 3) each of which entail an equilibration run of $1.5 \cdot 10^6 \Delta t$ and a production run of $10^6 \Delta t$. Compressions are made up to $\rho_g = 0.67$, which is found to be a crystalline state for all k_θ. Expansion sequences are performed in an equivalent, but reverse, manner from each $\rho_g = 0.67$ state. The resultant phase diagram is shown in Figure 3. To examine the sensitivity of the phase diagram simulations with different system sizes from $N \approx 1750$ to $N \approx 10,000$ are performed as well. These show only modest changes in the phase diagram in regard to system size and box shape. We therefore conclude that the very small crystallographic moduli at play here mean that commensurability effects, whilst obviously present, are surprisingly weak.

Phase identification is based on four main observables. The first of these was the excess pressure

$$p_{ex} = \frac{1}{3V_{box}} \sum_{i=1}^{N} \sum_{j>i}^{N} r_{ij} f_{ij} \qquad (2)$$

which is based on the virial and dependent of the distance r_{ij} of the center positions and the forces f_{ij} between particles i and j. All forces f_{ij} are repulsive, since the PHGO model is a soft-repulsive particle model [17, 43]. The excess pressure,
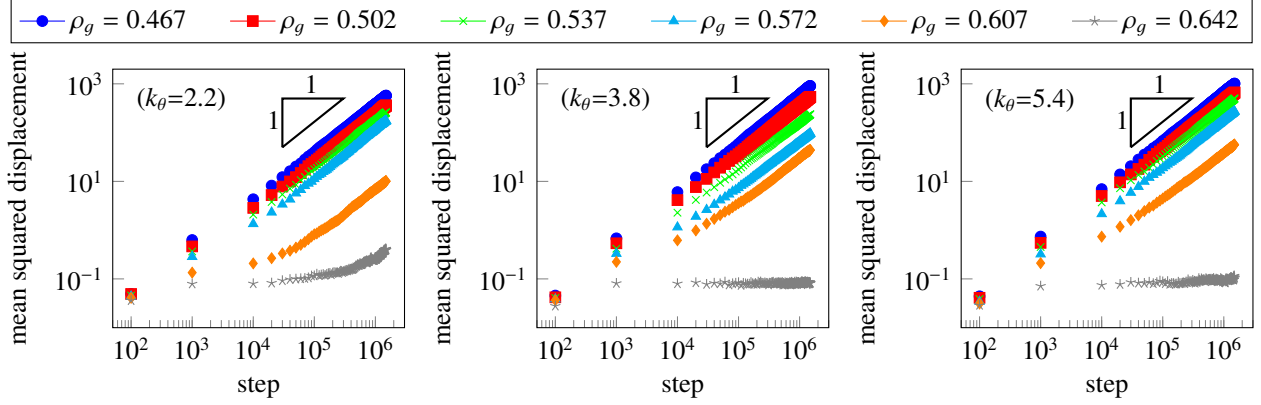
Figure 4. The mean squared displacement at different global densities for $k_\theta = 2.2$ (left), $k_\theta = 3.8$ (center) and $k_\theta = 5.4$ (right). A slope of 1 implies diffusive behaviour. At a density of $\rho_g = 0.546$ with $N = 3040$ particles the mean squared displacement of 20.84 σ_p corresponds to a displacement of the linear size of the simulation box. Depending on the phase parameters, such a displacement is achieved by a number of steps between $\approx$90000 steps (smectic, $k_\theta = 2.2$) to $\approx$160000 (Gyroid, $k_\theta = 3.8$).

however, has to be treated with caution, as we deal with a potential close to the hard core limit (maximally 2% overlap), in which p_{ex} is constant. The second key observable is the nematic order parameter

$$P_2 = \frac{1}{N} \sum_{i=1}^{N} (\frac{3}{2}(u_i \cdot n) - \frac{1}{2})$$

(3)

where u_i denotes the orientation vector of the ith particle and the system director, n, is the eigenvector associated with the largest eigenvalue of the tensor

$$Q = \frac{3}{2} \sum_{i=1}^{N} \left(u_i u_i - \frac{1}{3}\mathbb{1} \right).$$

(4)

The standard deviation of local orientations

$$\sigma(\alpha_i) = \sqrt{\frac{1}{N-1} \left[\left(\sum_{i=1}^{N} \alpha_i^2 \right) - \frac{1}{N} \left(\sum_{i=1}^{N} \alpha_i \right)^2 \right]},$$

(5)

based on the scalar product $\alpha_i = u_i \cdot u_j$ of the orientation vectors of nearest-neighbour particles i and j, and the diffusion coefficient D are the other main observables. D is determined from the diffusive-regime slope of the mean squared displacement characteristics such as those shown in Figure 4. These observables also serve to confirm system equilibration through their constancy under consideration of fluctuations within production runs (see Figure 5). Additionally, systems are analysed using cluster identification algorithms applied to the pear blunt ends, performed to enable structural characterisation of phases. From this, 6 distinct phases are identified - isotropic, nematic, smectic, Gyroid, solid smectic and solid Gyroid - as well as narrow biphasic or hysteretic regions (marked in grey on Figure 3) between isotropic and ordered fluid phases. Since the resultant phase diagram, Figure 3, can readily be divided into three sections with regard to the particle tapering parameter k_θ, details of observable characterisation are now given in the three Sections 2.1–2.3.

2.1 Strong particle tapering: $2.0 < k_\theta < 2.4$

For small tapering parameter, between $k_\theta = 2.0$ and $k_\theta = 2.4$, systems have low orientational order at low densities, $\rho_g = 0.49$ ($k_\theta = 2.0$) and $\rho_g = 0.52$ ($k_\theta = 2.4$), and cluster algorithms can not identify any full bilayer structures. However, randomly oriented bilayer-like clusters of interdigitating particles, such as those apparent in Figure 6 (center), are observed as the ordered phase is approached from low density.

On compression from the isotropic, the system exhibits smectic lamellar and solid-smectic phase behaviours. Whilst the excess pressure is an effective indicator of the transition from isotropic to smectic lamellar (Figure 5), the main signal of this transition is the adoption of high orientational order parameter (see Figure 5b). As depicted in Figure 6 (left), in the smectic phase, layers of interdigitating bilayer sheets or leaflets are formed in which all particles are orientationally aligned either parallel or antiparallel to one another. At intermediate densities, mobility remains diffusive, particle
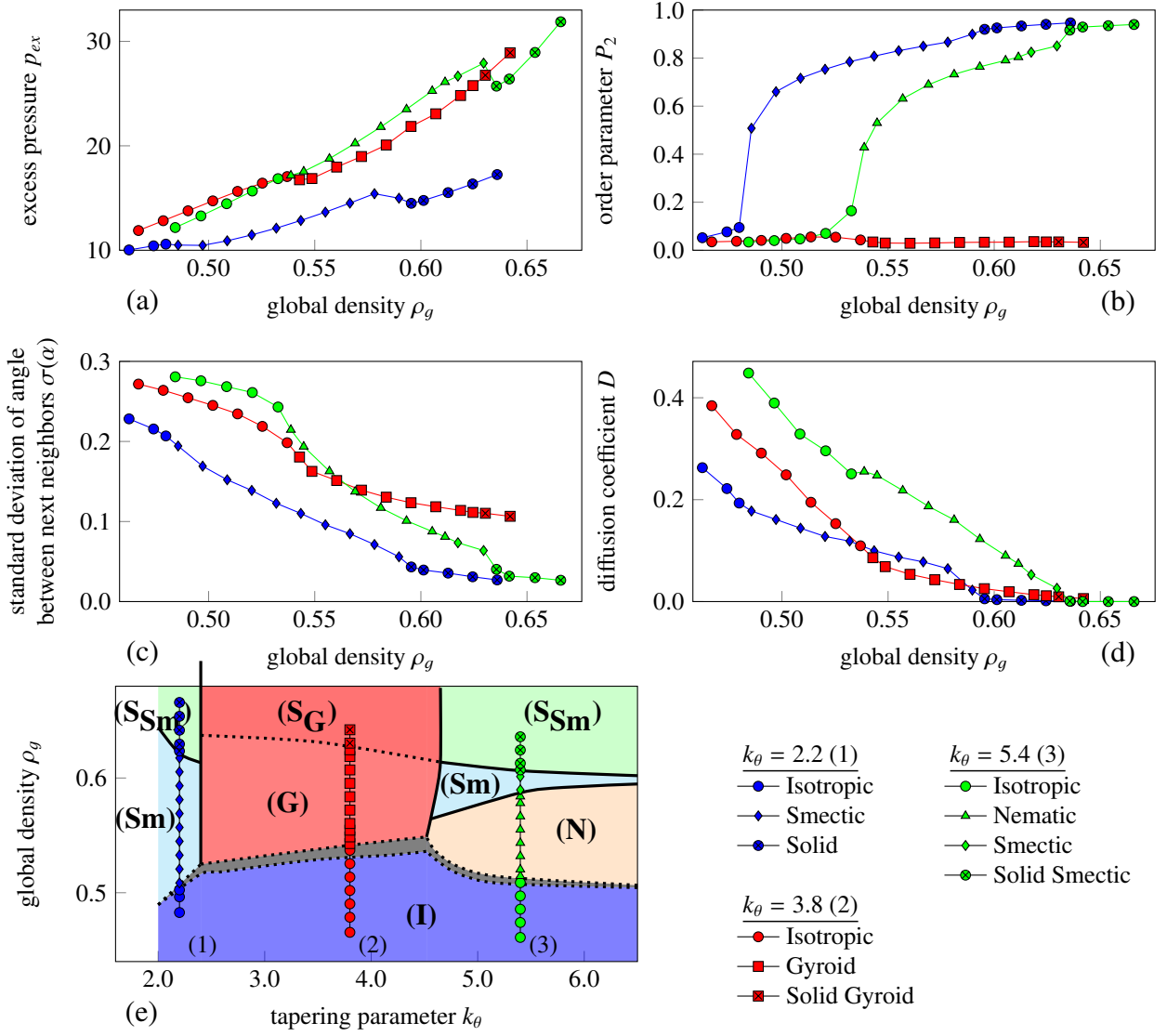
Figure 5. (a) The excess pressure p_{ex} (Eq. (2)), (b) nematic order parameter P_2 (Eq. (3)), (c) standard deviation of angles between nearest neighbour particles $\sigma(\alpha)$ (Eq. (5)) and (d) diffusion coefficient D obtained from the compression sequences of $k_\theta = 2.2$ (strong particle tapering), $k_\theta = 3.8$ (intermediate particle tapering) and $k_\theta = 5.4$ (weak particle tapering) particles, as depicted in (e). The diffusive character of the isotropic (I), nematic (N), smectic (Sm) and Gyroid phase (G) and the non-diffusive character of both solid phases (S_{Sm} and S_G) are shown by the mean squared displacement in Figure 4. All observables are obtained by both MD and MC simulation with the exception of D (MD only).

motion being dominated by in-leaflet diffusion but also involving occasional 'flip-flop' of pear-shaped particles between neighbouring sheets. A second transition, between smectic and solid-smectic, is characterised by a steep drop in mobility (see Figure 5d) as well as features in the excess pressure and order parameter characteristics.

2.2 Intermediate particle tapering: $2.4 < k_\theta < 4.5$

Pears with intermediate tapering, $2.4 < k_\theta < 4.5$, form an isotropic fluid for small values of ρ_g. However, as the density is increased for these systems, the Gyroid arrangement is adopted rather than the bilayer smectic phase. The isotropic-Gyroid transition occurrs at densities of between $\rho_g = 0.52$ ($k_\theta = 2.4$) and $\rho_g = 0.55$ ($k_\theta = 4.5$), the systems adopting a super-structure characterised by two interpenetrating channel networks (see Figure 7). The interdigitating curved bilayers indicate a smectic order on the Gyroid minimal surface (note related work on possible nematic ordering in block copolymers [45]). In this phase, the pear-shaped particles are able to traverse the simulation box isotropically, through both in-leaflet diffusion and leaflet to leaflet flip-flop. In addition to being bicontinuous and triply periodic, clusters identified from the positions of the blunt ends of the pears display nodes with three branch junctions, as is
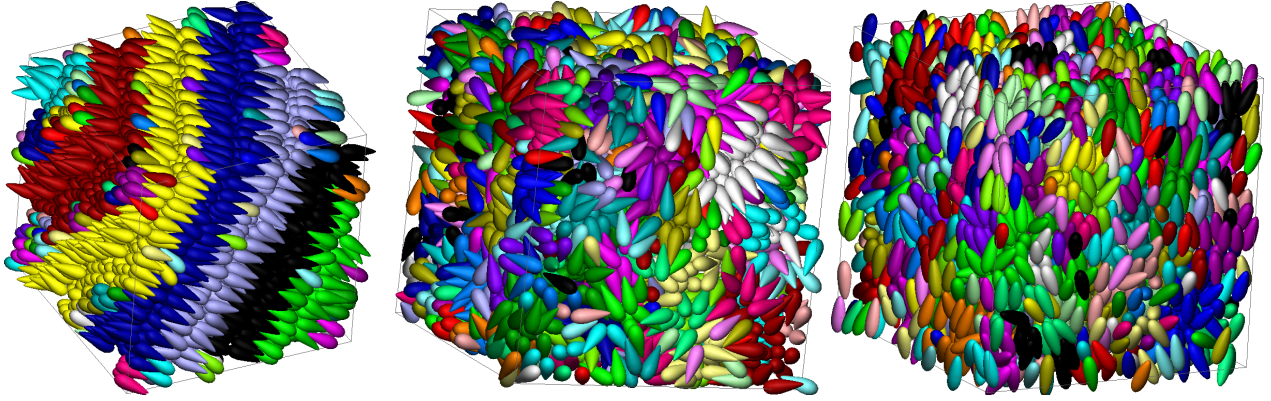
Figure 6. Representative configurations of 3040 pear-shaped particles forming the smectic lamellar (left: $k_\theta = 2.2$ $\rho_g = 0.59$), isotropic (center: $k_\theta = 2.2$ $\rho_g = 0.50$) and nematic (right: $k_\theta = 5.4$ $\rho_g = 0.53$) phases. Color coding of particles is used to indicate clusters calculated based on the proximity of pear blunt ends.
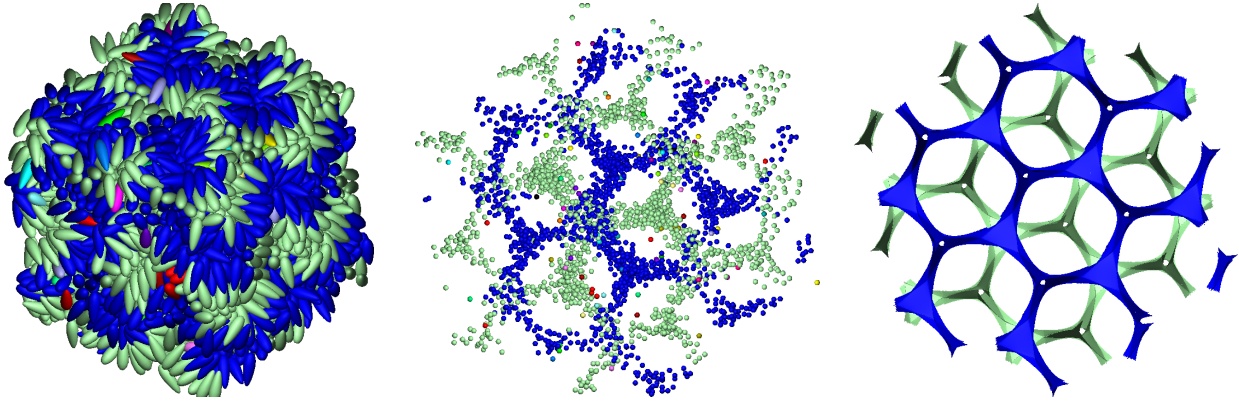

Figure 7. Left: Representative system of 3040 pear-shaped particles forming the Gyroid structure ($k_\theta = 3.8$ $\rho_g = 0.57$). Center: The positions of the blunt ends of the pears are depicted by spheres which are color coded to denote clusters calculated based on the proximity of pear blunt ends. Right: The two medial surfaces of the Gyroid surface [47].

characteristic for the double Gyroid. These clusters are, indeed, readily identifiable with the medial surface of the Gyroid. This medial surface (or axis) is a geometric construction that produces a centered skeleton of the original shape (see [46] for a recent review). For the case of bicontinuous structures, it represents a generalised line graph that also provides a robust definition of local domain (or channel) size and hence relates to questions of chain stretching frustration and geometric homogeneity [47–49]. For an object defined by its bounding surface, for every surface point p with surface normal vector $n(p)$, the corresponding medial surface point is defined as $p + d(p) \cdot n(p)$, where $d(p)$ is the medial surface distance function which describes the distance from p to the corresponding center of the channel. The structure of this simulated Gyroid phase is analysed in greater detail in Section 3.

At the phase transition from the isotropic to the Gyroid phase, the orientational order parameters of these intermediate particle tapering systems remains low (Figure 5b) in sharp contrast to what is seen for strong and weak particle tapering. However, the associated drop in the standard deviation of local orientations $\sigma(\alpha)$ (Figure 5c) suggests that the systems has adopted short-range orientational order. The transition from isotropic to Gyroid phase is also indicated by a feature in the excess pressure (Figure 5a), which coincides with the point of inflection of $\sigma(\alpha)$. Entering the Gyroid phase is also associated with a decrease in the gradient of the diffusion coefficient with respect to density (Figure 5d). A second change in the diffusion characteristic is seen at $\rho_g = 0.62$, above which the pear particles no longer traverse the simulation box in the course of a production run and, so, the system is characterised as solid. Due to the kinetic nature of this method of ascertaining solidification, the transition between the diffusive and solid phase is not defined distinctly and, consequently, is indicated as a dotted line in the phase diagram. Compared to the crystallization of the smectic bilayers, the Gyroid systems remains diffusive for higher densities. This may be an indication that a kinetically inaccessible solid lamellar

arrangement is the true stable phase at these high densities.

Systems of pears simulated at the phase boundary between the smectic and Gyroid phases, i.e. those with $k_\theta = 2.4$, can not be unambiguously assigned to either phase since both run cycles (isotropic-smectic-solid and isotropic-Gyroid) are observed on re-running simulation sequences. At this apparent transition region between the smectic and Gyroid phases, some configurations show long-lived coexistence between regions of parallel and curved bilayers and commensurability with the periodic boundary conditions is an issue. To investigate this behaviour further a second phase diagram is generated by performing simulation sequences with changing k_θ and constant ρ_g (see Fig. 8). Even though this procedure of changing the shape of particles is hardly possible for experiments on hard particles, we follow this idea which is inspired by the 'molecular shape concept' in lipid self-assembly [50, 51]. In binary lipid-water mixtures, many facets of the phase diagram can be understood simply by the recognition that changes in pressure, salt concentration or temperature translate to changes of the shape of the individual molecules. Starting from smectic configurations with $k_\theta = 2.0$ the tapering parameter is increased by $\Delta k_\theta = 0.1$ steps until $k_\theta = 6.0$. Afterwards the tapering parameter is decreased again until the particles take their original shape. The disposition of the phases are similar compared to the phase diagram in Fig 3. However, the gray area indicates major hysteresis effects between the smectic/nematic and Gyroid phase, which mainly reduce the parameter space where the Gyroid phase forms. The hysteresis effect is more dominant for higher densities which suggests again that for these high densities lamellar structures are similarly stable as the Gyroid.
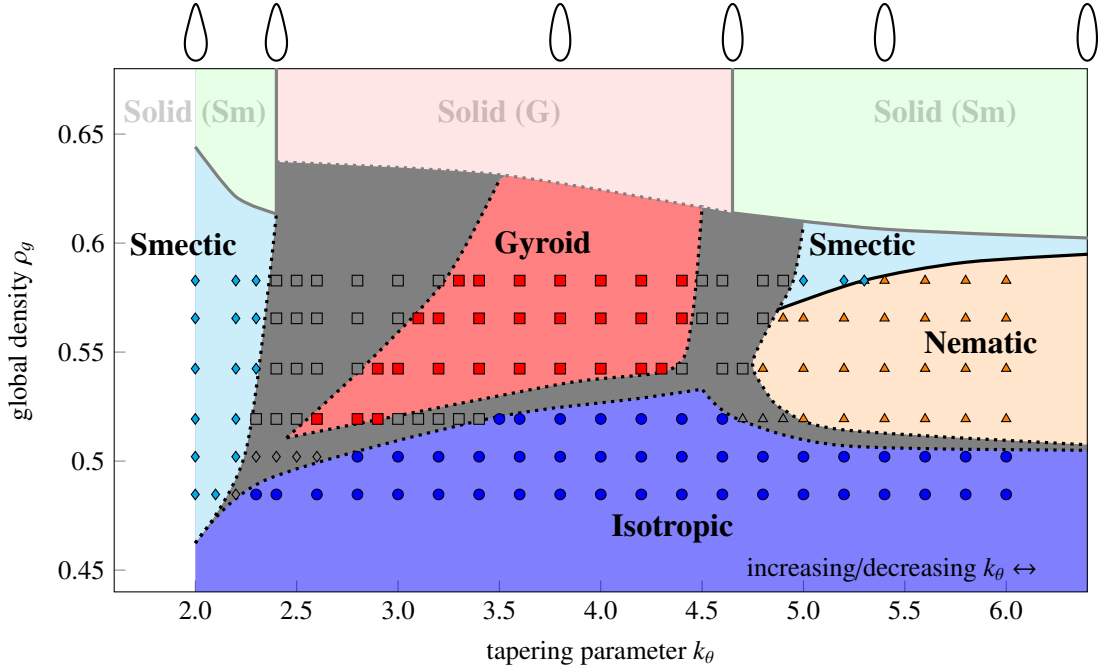

Figure 8. Phase diagram of hard pear-shaped particles with $k = 3.0$ obtained by increasing (from smectic) and decreasing k_θ at fixed global density ρ_g for systems of 3040 particles in a cubic simulation box. Gray regions between phases indicate parameter values for which phase hysteresis is observed between the increasing and decreasing sequences of k_θ. The schematics above the graph indicate the cross-sectional shape of the particles associated with each k_θ value. For the solid (dense) phases in Figure 3 it is not possible to dynamically adapt the particle shape.

2.3 Weak particle tapering: $k_\theta > 4.6$

For hard pear systems with $k_\theta > 4.6$, the simulations exhibit four different phases over the density range $0.46 < \rho_g < 0.65$. In addition to the solid-crystalline, smectic-lamella and isotropic phases formed by particles with small tapering parameter, these weakly tapered pears also adopt nematic order between the isotropic and smectic regions (see Figure 6). This window of nematic phase stability integrates straightforwardly into the phase diagram, as can be seen from the excess pressure and diffusion characteristics in Figure 5a+d, neither of which distinguish between the nematic and the Gyroid. We note from the phase diagram that the density range of smectic phase stability narrows as k_θ increases. This behaviour is expected since, for particles with $k_\theta \to \infty$ which represent ellipsoids, there is no smectic phase and systems exhibit transitions directly from the solid to the nematic phase [12].

Given that geometrical theories exist for phases, which are observed in lipid/water (shape parameter s [36]) and copolymer systems (strong segregation limit [52]), we compare the phase diagrams of lytropic [23, 50], AB diblock copolymer [30] and pear-shaped particle systems (see Figure 3 and 8). It is apparent that the phase diagrams exhibit both similarities and differences. Lipids with a shape parameter close to $s = 1$ and copolymers with a A-monomer fraction $f = 0.5$ generate lamellar macro structures, similar to weakly tapered hard pear-shaped particles. By decreasing s, f and k_θ, respectively, and making the particles more and more cone shaped, all three systems first transition into the bicontinous Gyroid phase. However, whereas close to $s = 0$ and $f = 0$ lipid/water and copolymer systems form cylindrical hexagonal phase structures and eventually spherical micelles, hard pear-shaped particles with small k_θ generate smectic (aka lamellar) structures again, which are, as already mentioned, characteristic for cylindrically shaped lipids and copolymers with $s = 1$ and $f = 0.5$.

3 Geometric analysis of the Gyroid structure

The simulations presented in Section 2 demonstrate that the Gyroid structure is formed by hard pears with tapering angles of between 12.4° and 23.5°. To draw further comparison between lipid/water, copolymer systems and the behaviour captured in our simulations, in the following Sections we characterise the unit cell of the hard-pear Gyroid structure, interrogate the microstructure of its minimal surface and perform Voronoi analysis to examine its underlying correlations.

3.1 Crystallographic lattice parameter and number of particles per unit cell

The triply periodic feature of the Gyroid dictates that its structure is determined by its periodicity. As a consequence, the simulations of the Gyroid phase presented in the previous Sections are subject to the commensurability issues encountered by any self-assembled system with crystallographic periodicity. In the thermodynamic limit, the lattice parameter a and the number N_{TUC} of particles within a translational unit cell result from thermodynamic equilibration. Fluctuations in the number of molecules in a unit cell or the size of that cell can then be accommodated since the total number of unit cells and the total number of molecules is infinite. In a simulation, by contrast, only a finite system volume can be modeled. In the hypothetical case where a and N_{TUC} are known *a priori*, the obvious choices would be to impose a simulation box with dimensions which are integer multiples of the translational unit cell, or an alternative (such as the one based on (110) and (001) directions described below) which represents a larger, differently oriented translational periodicity of the crystal structure. Where a simulation box is not both correctly oriented and commensurate with a and N_{TUC}, however, its behaviour would be distorted from that of the infinite system. The system might respond by forming defects, adopting a geometric structure that is not thermodynamically stable (but stabilised by the imposed simulation box), or attaining a modified version of the true equilibrium structure.

In practice, a and N_{TUC} are not known *a priori*, and the challenge lies in detecting rigorous estimates for these parameters from simulations of finite systems – and indeed determining beyond reasonable doubt that an observed geometric phase corresponds to the equilibrium (i.e., infinite) structure, rather than being stabilised by the finite simulation box. Even when the geometry is known, determining a and N_{TUC} from simulations is not straightforward. This problem has been considered in the context of cluster crystals [53] and a low-density low-temperature gyroid phase [35]; however, the methodology applied therein is not transferrable to our hard pear systems.[1] In the context of the results summarised in Figure 7 we note that, for $N = 3040$ particles with $k_\theta = 3.8$, a cubic simulation box with edge length $20.84\, w_p$ was required to form 8 unit cells of the Gyroid in a $2 \times 2 \times 2$ arrangement. However, from repeated compression sequences performed on a series of further simulated systems at the same number density ($\rho_g = 0.55$), we find that equivalent behaviour is obtained for a range of between 3000 and 3200 particles within the simulation box. To investigate these boundary-condition effects further, we therefore perform additional simulations with systems of 10,000 particles in an ensemble where the simulation box is able to adapt its three edge lengths independently whilst maintaining fixed total volume.

Using this approach to compress hard pear systems with $3.2 < k_\theta < 4.4$ to density $\rho_g = 0.555$ does not achieve mono-domain Gyroids in all cases. In particular, these large systems with $2.4 < k_\theta < 3.2$ prove prone to adopting poly-domain curvy bilayer structures, the particles of which can not be readily assigned to two independent channels using cluster analysis, even after $2 \cdot 10^7$ time-steps. Further, the crystallographic (100) direction of the Gyroids formed with particles $3.2 < k_\theta < 4.6$ are generally not aligned to the (1,0,0)-direction of the simulation box. However, by performing fast Fourier transformation of the density profile of the largest identifiable Gyroid domain and calculating the mean peaks of the resultant three dimensional scattering pattern, it proves possible to reliably determine the appropriate reciprocal lattice vectors of the FCC lattice in Fourier-space. From these, the lattice vectors of the Gyroid BCC lattice, the volume and consequently the number of particles within each unit cell N_{TUC} can be determined for each k_θ. A

---

[1]The method of Mladek *et al.* [53] relies on Widom's test particle insertion method [54, 55] to determine the chemical potential, but sampling efficiency for this approach is very poor for short-ranged repulsive potentials, particularly at the packing fractions of interest in this work.

representative structure of such a system ($k_\theta = 3.8$) is shown in Figure 1.
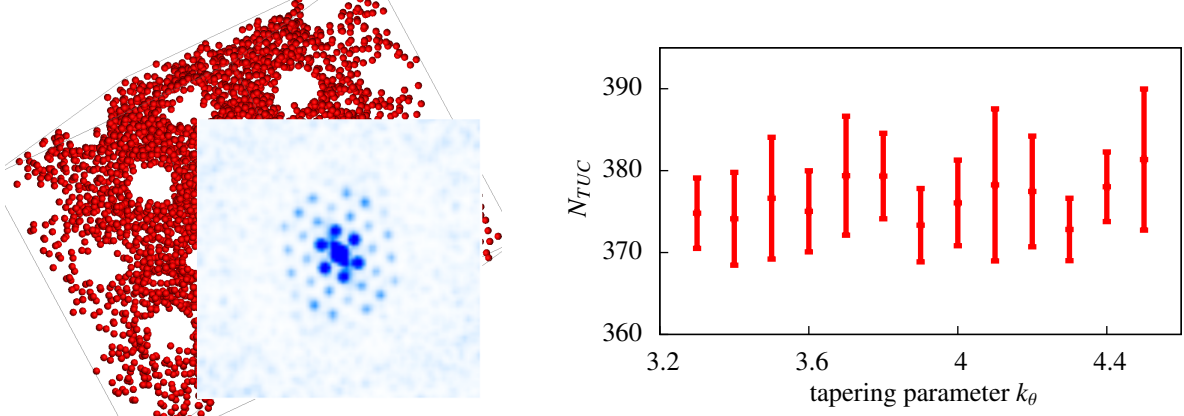

Figure 9. Left: The scattering pattern of the density distribution of a single channel in the Gyroid phase ($\rho_g = 0.555$). The cuboidal system contains 10000 pears with $k = 3$ and $k_\theta = 3.8$. Right: The number of particles for different tapering parameters are plotted.

This analysis of scattering functions is used to determine the k_θ-dependence of the mean and variance of the unit cell parameters (see Figure 9). These show that the tapering parameter has relatively little influence on the Gyroid unit cell, all systems yielding a particle number of 379±11. Whilst the corresponding scattering patterns show that some of the analysed cells are slightly elongated towards the (111) direction, the results of these Fourier analysed systems are in very good agreement with those from the $N = 3040$ simulations described in section 2 (see Figure 7). Additionally, single unit cell systems with $N = 380$ are simulated as depicted in Figure 11 where both channels contain a similar number of particles. Finally we generate systems of pears within a cuboidal simulation box with edge length ratio $\sqrt{2} : \sqrt{2} : 1$ and $N = 2N_{TUC} = 760$, which display both channel systems. In these, the x-axis points into the crystallographic (110), y into the (-110) and z into the (001) directions of the Gyroid.

Estimating the number of particles within the unit cell as $N_{TUC} = 379$ within the Gyroid phase at a density $\rho_g = 0.555$, the cubic lattice parameter is $a = 10.4$ in units of the width of the pears. It is instructive to compare the number N_{TUC} to that found in Gyroid-forming lipid systems. Using the fact that the surface area of the Gyroid minimal surface is $S = 3.0915 \times a^2$ and the average area of a single chain lipid such as monoolein is 37 Å^2 (at 25°C, [56]), we can estimate the number of lipid molecules in an $Ia\bar{3}d$ cubic Gyroid phase with lattice parameter $a = 140$Å to be $N = 2(3.0915 \times 140^2/37^2) \approx 89$ [57].

3.2 The Gyroid Minimal Surface

Having determined the unit cell size and shown, in Figure 1 and 7, that pear-shaped particles can be assigned to a channel system by cluster analysis of their blunt ends, we now consider another important aspect of the observed Gyroid phase – the characterization and analysis of its minimal surface. In binary lipid/water systems, lipids form sheets of bilayers such that the surfactant-water interfaces envelope the Gyroid minimal surface. The pears form bilayers as well, which have the same topology as the Gyroid. However, unlike lipid/water systems, the pear bilayers have to fully occupy space, such that the distance between the interpenetrating bilayers sheets has to be able to accommodate variable pore radii. As a result, the bilayer thickness cannot be assumed to be constant, and the distance between each pear center and the hypothetical interface which optimally bisects that bilayer has to be determined.

As a corrective we define a local particle-particle distance measure, called the local bilayer staggering length Δ, as the local distance between the centers of the two interpenetrating sheets. For this calculation, we consider the longitudinal distribution functions $g(z)$ of the double unit cell systems at a density of $\rho_g = 0.555$ to avoid possible errors caused by the deformed Gyroid in the 10,000 particles system. Here, z is the relative distance distribution between two pears measured along a particle rotational symmetry axis, and the calculation is restricted such that only pears within a cylinder of radius $0.9w_p$ around that axis are taken into account. This limiting radius is applied to ensure that pears from the same leaflet are excluded from the calculation. The resultant profiles are given in Figure 10.

We extract the local bilayer staggering length from the first peak attributed to the mean relative distance of two next neighbouring pears of interpenetrating sheets, measured along their rotational symmetry axes. The location of this peak
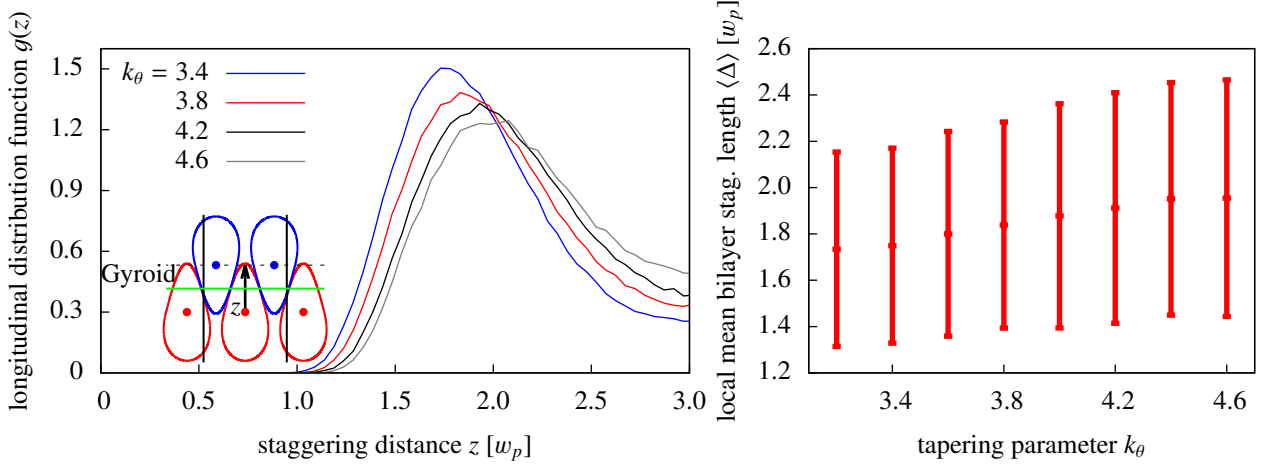
Figure 10. Left: The longitudinal distribution function of pear systems with 3040 particles at a density $\rho_g = 0.555$. Right: The mean distance between the center of the particles and the Gyroid minimal surface for different tapering parameter. The error bars indicate the full width at half maximum of the first peak. Note that the systems with $k_\theta = 3.2$ and $k_\theta = 4.6$ do not generate a Gyroid but a curved bilayer and nematic structure, respectively. These structures are, nevertheless, regarded as representative since they reflect the corresponding changes in bilayer thickness and pear locations.

shifts to larger z with increase in k_θ (The error bars in Figure 10 indicate the full width at half maximum of the first peak in $g(z)$ rather than the measurement error). This shift implies that particles with smaller tapering parameter, and consequently a higher tapering angle, interpenetrate more deeply, hence implying a smaller distance between these sheets. The width of the first peak shows that, for all systems, Δ is not constant within the Gyroid. This is analysed in further detail in section 3.3. The $g(z)$ curves are terminated before their second peak, which would correspond to the distance between the two bilayers. This is because curvature of the sheets introduces unacceptable levels of uncertainty in the data at this range of z. The other noteworthy trend in Figure 10 is that the peak heights drop and the tail at intermediate z grows with increase in k_θ. This, indicates that reducing the pear tapering angle broadens the distribution of observed stagger distances. Finally, we recall that these observations are made in the context that, as noted in Section 3.1, the overall unit cell size does not change with the tapering parameter.

3.3 Voronoi tessellation

In this Section we investigate the relationship between particle packing and minimal surface curvature in our simulated Gyroid phase. The Gyroid surface is characterised by its mean curvature $H = \frac{1}{2}(\kappa_1 + \kappa_2) = 0$ with the principal curvatures κ_1 and κ_2. Consequently, the Gauss curvature $K = \kappa_1 \cdot \kappa_2 \leq 0$ and, more precisely, its absolute value $|K|$ can be used to quantify curvature. Two approaches are used to relate this measure to simulation configurations. Firstly, multiple configurations are taken from simulations of freely self-assembled single unit cell structures generated by $N = 380$ particles. Secondly, unit cells are constructed using a Monte Carlo algorithm which induce the Gyroid structure by artificially restricting the pears to the Gyroid surface. In Figure 11 (left) the channel systems of the restricted and translated self assembled unit cell are separated by the Gyroid minimal surface parametrised by the Enneper-Weierstrass representation [58, 59]. We note that the two systems are qualitatively indistinguishable.

The local density

$$(\rho_l)_i = \frac{V_{pear}}{V_i} \tag{6}$$

around the i-th pear is proportional to the inverse volume of the Set Voronoi cell V_i of particle i, see Figure 11 (right). The Set Voronoi cell is defined as the space containing all points which are closer to the surface of a given particle than to any other particle in the system [60]. To calculate correlations between these cells and the Gyroid, the minimal surfaces shown in Figure 11 are triangulated and tessellated according to their intersections with the configuration-derived Voronoi diagrams. As a result, characteristics of the Voronoi diagram and the Gyroid are assigned to every point/triangle on the minimal surface. In Figure 12 the local Gauss curvature and the mean (from 1000 configurations) volume of intersecting Voronoi cells are, respectively, depicted on two Gyroid minimal surfaces. From this, it is apparent that highly curved regions at the necks of the Gyroid tend to be intersected by cells with higher volume, whereas more tightly packed particles reside in lower curvature zones (particularly the nodes). This can be interpreted as meaning that higher curvature required lower particle density since this avoids the restrictions otherwise associated with leaflet interdigitation. To
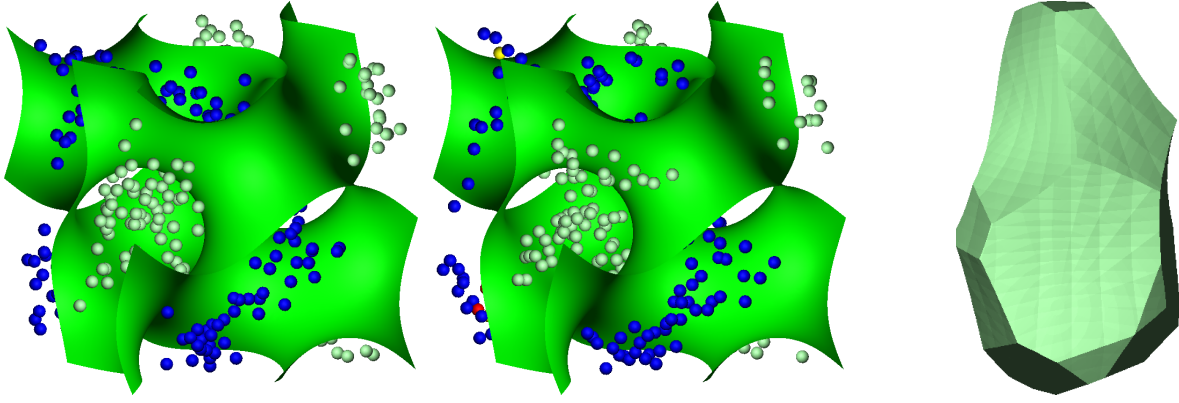
Figure 11. The channel systems of unit cells, depicted by the position of the blunt ends of particles with $k = 3$ and $k_\theta = 3.8$ ($\rho_g = 0.555$). Left: The Gyroid created by Monte Carlo simulation with particles restricted to the nodal approximation $|\sin(x) \cdot \cos(y) + \sin(y) \cdot \cos(z) + \sin(z) \cdot \cos(x)| < \epsilon$ in such a way that the particles cut the Gyroid surface within the range of ϵ at the distance determined in section 3.2 and Figure 10. Also their orientations are constrained to lie close to the nodal surface normal (in the range of $\pm 10°$) at all Monte Carlo steps. Center: The equivalent unit cell surface generated by unrestricted self-assembly of $N - 380$ hard pears. The scattering functions (see Figure 9) of the restricted and the unrestricted self assembled unit cells can be compared by using an MC algorithm to maximise their correlation with respect to simulation box translation. Right: The Voronoi cell of a single pear particle within the unrestricted Gyroid phase.

achieve a more quantitative measure of this effect, the area A_0 occupied by each Voronoi cell is summarised in a plot of $\langle \frac{V}{A_0} \rangle$ against $|K|$ - an anti-correlation is observed (see Figure 13 left). Similarly, another anti-correlation is found when the Gauss curvature was, equivalently, plotted against the distance between the Gyroid surface and the pear positions (see Figure 13 right). This means that the pears remain further away from the minimal surface at the nodes than at the necks. These two anti-correlation are mutually consistent since low curvature in compatible with high interpenetration.
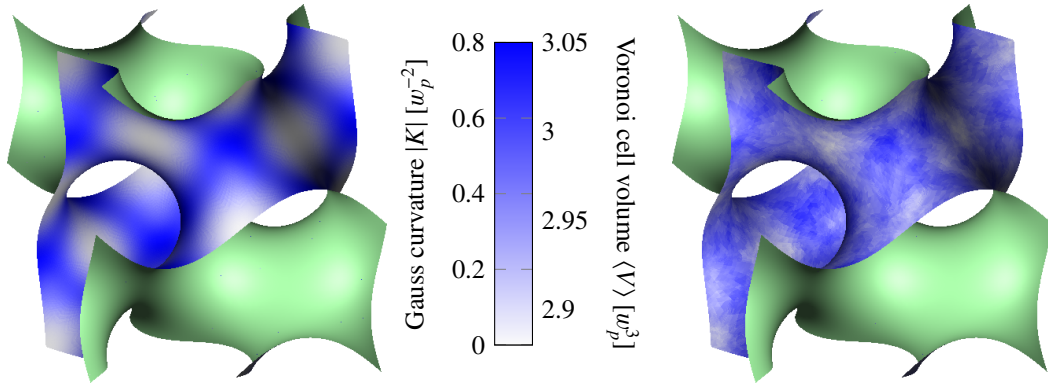

Figure 12. Left: The Gyroid surface colored by gaussian curvature. More curved areas are blue, less curved areas are white. Right: By comparison the Gyroid is colored in respect of the mean volume of intersecting Set Voronoi cells. Blue sections are intersected by cells with high volume whereas white sections are intersected by cells with low volume. For the calculation 1000 systems are used.

Comparing these findings for our pear systems with those for lipids and polymers, differences are apparent. The molecular geometry is described by the "surfactant parameter" $\frac{v}{A_0 \cdot l}$ where v is the effective surfactant chain volume and l is the chain length [23]. By invoking the relationship between molecular shape and resulting interface curvatures, one can then express the so-called Steiner's formula as:

$$v = A_0(l + H \cdot l^2 + \frac{1}{3} K \cdot l^3).\tag{7}$$

Lipids and copolymers which form the Gyroid surface are conventionally sketched as cones ($\frac{v}{A_0 \cdot l} < 1$), whereas in the lamella phase the molecules are considered as cylinders ($\frac{v}{A_0 \cdot l} = 1$) [23, 36]. This is illustrated in Figure 2. Plotting Steiner's formula in Figure 13 and analysing the shape of the tapered Voronoi cell of a single pear (see Figure 11 right), shows that the pear particles have a surfactant parameter greater than 1. However, whilst molecular flexibility means that

it is often feasible for lipids and copolymers to have differing surfactant parameters in opposing leaflets, this is patently *not* the case in the systems studied here. Due to the interdigitation and fixed particle shape in our hard pear systems (recall Figure 2) it is also necessary for pear blunt ends to point into the opposing channels. This violates Steiner's theorem, leading to the poor agreement between simulation data and equation 3.3 and leading us to conclude that the mechanisms behind the formation of the Gyroid by lipids/copolymers and hard pears may be different.
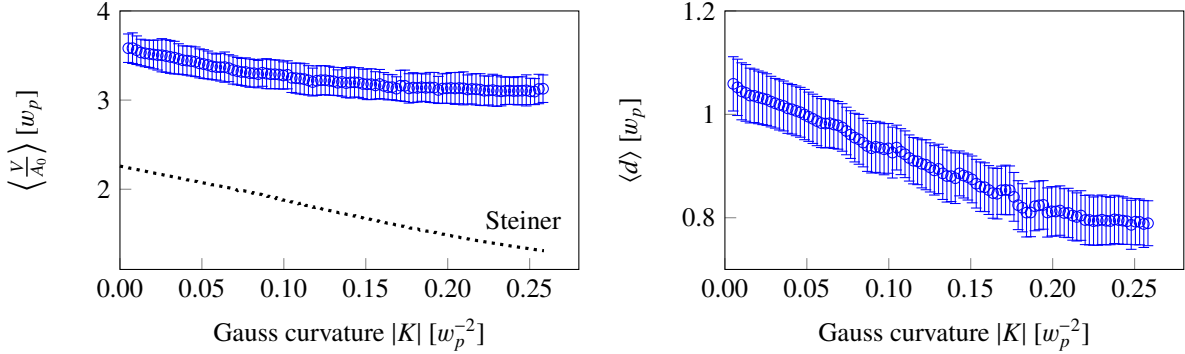

Figure 13. Gauss curvature of the Gyroid against mean volume of intersecting Set Voronoi cells (Left) and against mean distance between the center of the pear and the Gyroid surface $\langle d \rangle$ (Right) using pears with $k_\theta = 3.8$. Every point represents a triangle of the triangulated Gyroid surface. For the calculation 1000 systems are used. The dotted line indicates Steiner's theorem (Eq. 3.3), where $l = d_{MS}(p)$ is the distance between the point p on the Gyroid surface and its corresponding point on the medial surface (see section 2.2). The Gauss curvature $K(p)$ and $d(p)$ are calculated numerically using the Gyroid minimal surface parametrised by the Enneper-Weierstrass representation [58, 59]. The mean curvature $H(p)$ is 0 at every point p on a minimal surface.

4 Conclusion

We have simulated and numerically analysed systems of hard pear-shaped particles capable of forming the Ia$\bar{3}$d Gyroid phase. Through this, we have confirmed that attractive interactions are not necessary for the formation of this structure and that the Gyroid can be stabilised by purely entropic effects. The phase diagram obtained here indicates that particles with a range of tapering parameters, corresponding to tapering angles of between 12.4° and 23.5°, are able to form the Gyroid phase. Also structural analysis has been used to determine key characteristics of the Gyroid, such as the unit cell size and occupancy and the local bilayer staggering length. Correlations between the curvature of the Gyroid surface and the Voronoi cells of the pears have shown that a more open structure is adopted in areas of higher curvature, and that the Gyroid's range of channel widths are accommodated by variation in leaflet interpenetration.

It has been shown that Gyroids assembled by our pear systems differ from those generated by lipids in terms of the surfactant parameters appropriate to particles in the bilayer. Additionally, we note that the phase boundaries found here for the Gyroid are fundamentally different from those seen in many experimental systems. Conventionally, the Gyroid is sandwiched between planar lamellar and hexagonal phases, and its stability is argued in terms of curvature elasticities. This, though, is difficult to reconcile with the phase diagram of Figure 3, in which the Gyroid borders isotropic and nematic fluids for which there is no curvature elasticity. A possible explanation for this is offered by recent arguments from the Selinger group [61] that sufficiently strong bulk splay-bend coupling between polar and orientational degrees of freedom can destabilise the nematic with respect to supra-molecular modulations (i.e. periodic structures). These arguments, in turn, hark back to the classic paper of Dozov [62] in which the central ideas of the twist-bend nematic were set out. Given that our hard pear systems clearly possess steric coupling between molecular-scale splay and bend, there appears to be a strong argument that the Gyroid region observed here is indeed a realisation of a modulated splay-bend phase predicted by Dozov and Selinger.

In general it is interesting to further investigate if it is possible to self assemble other cubic phases purely entropically – like the polar blue phase, which is predicted for liquid crystals [61], or other minimal surface phases (note recent work on quenched polymeric phases [63–65], including simulations of bicontinuous structures [64, 65]). Here it is advisable to be guided by biological systems again and to introduce a second component such as an oligomer or a solvent of hard spheres, which might promote a change in curvature. Alternatively, approaches based on polydisperse systems and active particles may prove effective in influencing mesoscopic structure. The aim here would be to partition space into cells according to a given target desired structure with, preferably, small variation in total volume. This idea is the entropic

equivalent to designing potentials which induces particle clustering [66]. In pursuing such a goal, the approach of Section 3.3 of restricting particles to a given minimal surface and tracking their behaviours, might prove useful.

A recurrent question in the context of Gyroid-like phases is chirality, discussed in particular in terms of optical properties [67–69] and in terms of an observed, but unexplained enantiomeric imbalance in butterfly Gyroid nanostructures [70, 71]. While the hard-pear system described here adopts only the achiral Gyroid phase with symmetry $Ia\bar{3}d$, it may also inform on the issue of chiral generalisations. While synthetic self-assembly protocols exist to generate chiral single Gyroids with symmetry $I4_132$ [72] or solid replicas thereof [68], these do not break the chiral symmetry, that is, left-handed and right-handed enantiomers occur with equal probability. In these systems, the two network-like domains are chemically distinct, say A and C, yet the probability for A and C to be the right-hand Gyroid network is equal at 50:50 (Note that more complicated chiral Gyroid-like arrangements have been observed in simulations [73] or analysed in terms of geometric free energy concepts [74]). The open question is what is required to make the A moiety adopt the, say, right-handed network with a higher probability than the left-handed one. It has been demonstrated that molecular twist in copolymeric components can affect the mesoscopic structural chirality (and enantiomeric type) of the self-assembled nanostructure [75]. The $Ia\bar{3}d$ Gyroid phase described here is interesting in the sense that the pears naturally subdivide into two groups, each occupying one of the two labyrinthine domains. It is, though, conceivable that a small adaption of the particles to embed chiral character may lead to an adapted mesoscale geometry (where the labyrinthine domain that 'matches' one particle enantiomeric type is different from the other, e.g. higher density); only one of the two enantiomers of the $I4_132$ Gyroid would then form. Further, if a mixture of both enantiomeric particle types were considered, it is conceivable that a chiral microphase separation may result, with RH particles occupying the RH domain and LH particles the LH domain, again producing only one of the two enantiomers of the $I4_132$ single Gyroid. While such demixing is unlikely, due to entropy, it is not impossible, and so would be a fascinating topic for future research.

Acknowledgements

References

[1] M. Kardar, *Statistical physics of particles* Cambridge University Press, p. 51 (2007)

[2] R. K. Pathria and P. D. Beale *Statistical Mechanics* **3** Elsevier, p. 5 & 52 (2011)

[3] D. P. Landau and K. Binder *A guide to Monte Carlo simulations in statistical physics* Cambridge University Press, p. 9 (2014)

[4] B. J. Alder and T. E. Wainwright, J. Chem. Phys. **27**, 1208 (1957)

[5] W. G. Hoover and F. H. Ree, J. Chem. Phys. **49**(8), 3609–3617 (1968)

[6] P. N. Pusey and W. Van Megen, Nature **320**(6060), 340–342 (1986)

[7] S. C. Kapfer and W. Krauth, Phys. Rev. Lett. **114**, 035702 (2015)

[8] E. P. Bernard and W. Krauth, Phys. Rev. Lett. **107**, 155704 (2011)

[9] H. Hansen-Goos and K. Mecke, Phys. Rev. Lett. **102**, 018302 (2009)

[10] E. Fischermeier, D. Bartuschat, T. Preclik, M. Marechal and K. Mecke, Comput. Phys. Commun. **185**(12), 3156–3161 (2014)

[11] J. A. C. Veerman and D. Frenkel, Phys. Rev. A **41**, 3237–3244 (1990)

[12] D. Frenkel, B. M. Mulder and J. P. McTague, Phys. Rev. Lett. **52**, 287 (1984)

[13] H. B. Kolli, E. Frezza, G. Cinacchi, A. Ferrarini, A. Giacometti, T. S. Hudson, C. De Michele and F. Sciortino, Soft Matter **10**, 8171 (2014)

[14] G. Few and M. Rigby, Chem. Phys. Lett. **20**, 433–435 (1973)

[15] M. Dennison, K. Milinković and M. Dijkstra, J. Chem. Phys. **137**, 044507 (2012)

[16] V. N. Manoharan, Science **349**, 1253751 (2015)

[17] F. Barmes, M. Ricci, C. Zannoni, and D. J. Cleaver, Phys. Rev. E **68**, 021708 (2003)

[18] L. J. Ellison, D. J. Michel, F. Barmes, and D. J. Cleaver, Phys. Rev. Lett. **97**, 237801 (2006)

[19] A. H. Schoen, NASA Technical Note TN D-5541 (1970)

[20] A. H. Schoen, Interface focus **2**(5), 658–668 (2012)

[21] K. Grosse-Brauckmann, J. Colloid Interface Sci. **187**, 418–428 (1997)

[22] S. T. Hyde and G. E. Schröder-Turk, Interface Focus **2**(5), 529–538 (2012)

[23] S. T. Hyde, Z. Blum, T. Landh, S. Lidin, B. W. Ninham, S. Andersson and K. Larsson, *The language of shape: the role of curvature in condensed matter: physics, chemistry and biology* Elsevier (1996)

[24] S. T. Hyde, M. O'Keeffe and D. M. Proserpio, Angew. Chem. Int. Ed. **47**(42), 7996–8000 (2008)

[25] S. T. Hyde and S. Andersson, Z. Kristallogr. Cryst. Mater. **168**(1-4), 213–220 (1984)

[26] K. Larsson, J. Phys. Chem. **93**(21), 7304–7314 (1989)

[27] J. M. Seddon and R. H. Tepler, Phil. Trans. R. Soc. A **344**(1672), 377–401 (1993)

[28] V. Luzzati and P. A. Spegt, Nature **215**, 701–704 (1967)

[29] D. A. Hajduk, H. Takenouchi, M. A. Hillmyer, F. S. Bates, M. E. Vigild and K. Almdal, Macromolecules **30**(13), 3788–3795 (1997)

[30] M. W. Matsen and M. Schick, Phys. Rev. Lett. **72**(16), 2660 (1994)

[31] D. A. Hajduk, P. E. Harper, S. M. Gruner, C. C. Honeker, G. Kim, E. L. Thomas and L. J. Fetters, Macromolecules **27**(15), 4063-4075 (1997)

[32] X. B. Zeng, G. Ungar, and M. Impéror-Clerc, Nat. Mater. **4**, 562 (2005)

[33] A. Ciach, Phys. Rev. E **78**(6), 061505 (2008)

[34] M. Edelmann and R. Roth, Phys. Rev. E **93**, 062146 (2016)

[35] Y. Zhuang, K. Zhang and P. Charbonneau, Phys. Rev. Lett. **116**, 098301 (2016)

[36] J. N. Israelachvili, D. J. Mitchell and B. W. Ninham, J. Chem. Soc., Faraday Trans. 2 **72**, 1525-1568 (1976)

[37] W. Helfrich, Z. Naturforsch. C **28**, 693 (1973)

[38] U. S. Schwarz and G. Gompper, Phys. Rev. Lett. **85**(7), 1472 (2000)

[39] Anton Chekhov (c.1900)

[40] J. D. Weeks, D. Chandler, and H. C. Andersen, J. Chem. Phys. **54**, 5237 (1971)

[41] D. J. Cleaver, C. M. Care, M. P. Allen and M. P. Neal, Phys. Rev. E **54**(1), 559 (1996)

[42] J. W. Perram, J. Rasmussen, E. Præstgaard and J. L. Lebowitz, Phys. Rev. E **54**(6), 6565 (1996)

[43] R. Berardi, M. Ricci and C. Zannoni, ChemPhysChem **2**(7), 443–447 (2001)

[44] D. Frenkel and B.Smit, *Understanding Molecular Simulation: From Algorithms to Applications* Computational Science Series, Academic Press, 9–12 (2002)

[45] I. Prasad, Y. Seo, L. M. Hall and G. M. Grason, arXiv:1612.07994 (2016)

[46] A. Tagliasacchi, T. Delame, M. Spagnuolo, N. Amenta and A. Telea, Comput. Graph. Forum **35**(2), 573–597 (2016)

[47] G. E. Schröder, S. J. Ramsden, A. G. Christy and S. T. Hyde, Eur. Phys. J. B **35**(4), 551–564 (2003)

[48] G. E. Schröder-Turk, A. Fogden and S. T. Hyde, Eur. Phys. J. B **54**(4), 509–524 (2006)

[49] G. E. Schröder-Turk, A. Fogden and S. T. Hyde, Eur. Phys. J. B **59**(1), 115–126 (2007)

[50] S. T. Hyde, *Identification of Lyotropic Liquid Crystalline Mesophases* Handbook of Applied Surface and Colloid Chemistry, Wiley, Chapter 16 (2001)

[51] B. W. Ninham, K. Larsson and P. Lo Nostro, Colloids Surf. B **152**, 326–338 (2017)

[52] A. N. Semenov, Macromolecules **26**(24), 6617–6621 (1993)

[53] B. M. Mladek, P. Charbonneau and D. Frenkel, Phys. Rev. Lett. **99**, 235702 (2007)

[54] B. Widom, J. Chem. Phys. **39**, 2808 (1963)

[55] J. Powles, W. Evans and N. Quirke, Molec. Phys. **46**, 1347 (1982)

[56] H. Chung and M. Caffrey, Biophysical journal, **66**(2), 377 (1994)

[57] G. C. Shearman, O. Ces, R. H. Templer and J. M. Seddon, J. Phys.: Condens. Matter **18**, 1105–1124 (2006)

[58] J. C. C. Nitsche, *Lectures on Minimal Surfaces* **1** Cambridge University Press (1989)

[59] P. J. F. Gandy and J. Klinowski, Chem. Phys. Lett. **321**, 363–371 (2000)

[60] F. M. Schaller, S. C. Kapfer, M. E. Evans, M. J. F. Hoffmann, T. Aste, M. Saadatfar, K. Mecke, G. W. Delaney and G. E. Schröder-Turk, Philos. Mag. **93**(31-33), 3993-4017 (2013)

[61] S. M. Shamid, D. W. Allender and J. V. Selinger, Phys. Rev. Lett. **113**(23), 237801 (2014)

[62] I. Dozov, Europhysics Letts. **56**(2), 247-253 (2001)

[63] S. Lee, C. Leighton and F. S. Bates, PNAS **111**(50), 17723–17731 (2014)

[64] M. Müller and D. W. Sun, Phys. Rev. Lett. **111**(26), 267801 (2013)

[65] D. W. Sun and M. Müller, Phys. Rev. Lett. **118**(6), 067801 (2017)

[66] H. Shin, G. M. Grason and C. D. Santangelo, Soft Matter **5**, 3629 (2009)

[67] M. Saba, B. D. Wilts, J. Hielscher and G. E. Schröder-Turk, Mater. Today Proc. **1**, 193–208 (2014)

[68] S. Vignolini, N. A. Yufa, P. S. Cunha, S. Guldin, I. Rushkin, M. Stefik, K. Hur, U. Wiesner, J. J. Baumberg and U. Steiner, Adv. Mater. **24**(10), OP23–OP27 (2012)

[69] S. S. Oh, A. Demetriadou, S. Wuestner and O. Hess, Adv. Mater. **25**(10), 612–617 (2013)

[70] B. Winter, B. Butz, C. Dieker, G. E. Schröder-Turk, K. Mecke and E. Spiecker, PNAS **112**(42). 12911-6 (2015)

[71] C. Mille, E. C. Tyrode and R. W. Corkery, RSC Adv. **3**(9), 3109–3117 (2013)

[72] T. H. Epps, E. W. Cochran, T. S. Bailey, R. S. Waletzko, C. M. Hardy and F. S. Bates, Macromolecules **37**(22), 8325–8341 (2004)

[73] J. J. K. Kirkensgaard, M. E. Evans, L. de Campo and S. T. Hyde, PNAS **111**(4), 1271–1276 (2014)

[74] G. E. Schröder-Turk, L. de Campo, M. E. Evans, M. Saba, S. C. Kapfer, T. Varslot, K. Grosse-Brauckmann, S. Ramsden and S. T. Hyde, Faraday Discuss. **161**, 215–247 (2013)

[75] W. Zhao, T. P. Russell and G. M. Grason, Phys. Rev. Lett. **110**(5), 058301 (2013)